



Contributions of constraints to mechanical fields of energy pile foundation

Hassan Abbaszadeh Amirdehi¹ · Issa Shooshpasha¹

Received: 20 December 2022 / Accepted: 5 April 2023 / Published online: 24 April 2023
© Springer Nature Switzerland AG 2023

Abstract

In most practical cases, the free deformation tendency of energy piles is constrained by the cap and surrounding soil. As a result of these constrained thermal deformations, additional forces are introduced into the system and are balanced by transfer to the ground via soil-structure interfaces. Consequently, interface conditions and structural element constraints play crucial roles in the behavior of energy pile foundations, and their evaluation is essential. This study evaluates the effects of constraints on the response of a large-scale piled raft foundation in homogeneous stiff saturated clay to cyclic thermal loads using coupled Thermo-Hydro-Mechanical Finite Element modeling. Particularly, the effects of interface stiffness and mechanical load variations in the evolution of mechanical fields, including stresses, displacements, and load-sharing ratios, were investigated. Despite the magnitude independence of the initial stresses, the greater constraining effect of the stiffer soil-structure interface and stronger pile-raft connection led to substantial excess loads, especially at shallow depths. Nevertheless, due to the performance of floating piles, the thermal axial stress variations in deep regions were virtually identical. Moreover, the larger tendency of the soil than the piles to undergo thermal deformations was found to be the primary determinant of the resultant load redistribution, which led to the soil-raft interface being a significant factor in determining vertical raft displacements. In the most severe case, the thermal axial stress variation range and stabilized excess settlement of the foundation were approximately three times the mechanical stress and one-fifth of the mechanical settlement, respectively.

Keywords Energy pile · Constraint effect · Interface stiffness · Cyclic thermal loading · Axial stress variation · Excess settlement

Introduction

Energy pile foundations are an innovative system that combines the geo-structural contributions of conventional pile foundations in resisting loads with geothermal heat exchange to provide energy to the superstructure. In addition to transferring structural loads to layers with greater load capacities, piles with direct access to shallow depths can exchange heat between the earth and superstructure by circulating the heat carrier fluid in concrete-embedded absorber pipes. Due to multifunctionality and simultaneous mechanical and thermal

loading, the design and analysis of energy pile foundations must consider the interdependent aspects of material behavior and Thermo-Hydro-Mechanical (THM) responses of system components [1–7].

In most practical cases, the free radial and longitudinal deformation tendency of energy piles caused by cyclic temperature changes is constrained by the cap and surrounding soil [8–10]. In the radial direction, volumetric contraction of soils decreases normal effective stress at the soil-pile interface, thus, reducing the shaft resistance [11, 12]. The reduced shaft resistance would be compensated by the increased base bearing of floating piles and load transfer through the pile cap [13, 14]. Although thermally induced pile length changes may result in additional mobilized friction along some parts, the reduction in shaft resistance due to the reduced normal effective stress may be a more dominant factor [15]. However, the soil acts as a restraint at the pile base and shaft, while the applied mechanical load and

✉ Issa Shooshpasha
shooshpasha@nit.ac.ir

Hassan Abbaszadeh Amirdehi
a.amirdehi@gmail.com

¹ Department of Civil Engineering, Babol Noshirvani University of Technology, Shariati Ave, Babol, Mazandaran, Iran

group effects due to pile-raft connection may constrain thermally induced elongation at the pile head [16].

In contrast to the significant constraints imposed by bedrock beneath end-bearing piles, the soil beneath the base of floating piles may impose constraints comparable to those imposed by the pile head. Consequently, ground stiffness conditions can influence the variations in foundation displacement and axial load along energy piles, and the mobilized strength change of the pile base is expected in response to thermal loading [17–20].

In addition to the applied mechanical load, the layout of energy piles in a group containing conventional piles also affects restraint at the pile heads, resulting in load redistribution [21]. The conventional piles not directly exposed to temperature changes impose constraints on pile head displacement corresponding to the pile-raft connection rigidity [22]. Thus, the thermomechanical load must be redistributed through the cap in each cycle between the conventional and energy piles [23].

According to the mechanisms described above, interface conditions and structural element constraints play fundamental roles in the behavior of energy pile foundations, and their assessment is essential. Numerous studies have examined the responses of energy pile foundations to combined loads via experimental tests [16, 24–30] and numerical analyses [9, 19, 31–43] to date. Nevertheless, a literature review demonstrated that existing parametric studies [5, 31, 36, 43, 44] have yet to comprehensively consider the effects of change in the constraint conditions of a foundation containing conventional and energy piles, despite its significant contribution to the system response under cyclic thermal loading. Hence, the impact of these variables under different stress states and both low and high operating temperatures is unknown. Therefore, validated numerical models, which are a potent tool for evaluating the behavior of energy piles over practical timescales and can simultaneously incorporate multiple aspects governing the physical THM phenomena, can be used to address this limitation.

This study primarily aimed to evaluate the constraints of energy pile foundations by quantifying the effects of soil structure and pile-raft interface stiffness and the mechanical load on mechanical fields. To this end, numerical coupled THM simulations were performed using the Finite Element (FE) modeling to evaluate the spatial and temporal evolution of stresses, displacements, and load-sharing ratio in a piled raft foundation in saturated stiff clay. In contrast to previous studies, the applied model incorporates several principal aspects of the actual physical phenomena simultaneously, including a) simulating interfaces with the possibility of slip rather than considering perfect contact conditions, b) considering ground temperature variations at shallow depths instead of the unrealistic assumption of uniform ground temperature, and c) assuming thermoelastic-plastic

soil response for the proper estimation of strains under all circumstances instead of considering elastic behavior. The results of this study will contribute to a better understanding of the mechanical behavior of energy pile foundations under varying constraint conditions, particularly in saturated stiff clay, and provide valuable information for structural design and superstructure serviceability. This will improve engineers' ability to design safe energy pile foundations.

The mathematical formulation and constitutive models will be described in the following sections. Afterward, the proposed model is validated by comparing numerical predictions to full-scale in situ tests. Finally, parametric analysis is provided to evaluate the previously mentioned key factors.

FE model

This study focuses on characterizing the change in model output because of the variation in model input parameters. Indeed, sensitivity analysis is a useful tool, which not only allows to understand how the model behavior depends on certain parameters but also indicates which parameter values are the most influence [45, 46]. Therefore, numerical analyses were performed to gain deeper insight into the effect and relative importance of constraint conditions with regard to geo-structural response behavior. Numerical simulations were implemented in COMSOL Multiphysics [47], which employs the FE method to convert the governing equations into numerically solvable algebraic equations. To quantitatively describe coupled phenomena during the thermal operation of energy piles in a pile foundation, it is required to incorporate mechanical, thermal, and hydraulic aspects into the model at the same time; material volume changes are dependent on temperature, heat transfer is dependent on groundwater flow possibility, water density changes with the thermal load, and the mechanical response of soil is dependent on the pore water pressure [34]. Therefore, the numerical modeling of the system requires a fully THM formulation that can be effectively implemented in the used software. The main focus is on thermally induced mechanical effects on the piles and surrounding soil for the normal operation of the geothermal heat pump system in realistic conditions, while the flow interaction within the pipes and its energy aspects were neglected.

Multiphysics contact problems are often very ill-conditioned, which leads to convergence problems for the nonlinear solver. In the COMSOL, there is a fully coupled method for solving Partial Differential Equations (PDEs) at each time-step that includes all of the couplings between the unknowns at once. Compared to other approaches, this method often converges in fewer iterations and is therefore preferred for solving systems of nonlinear equations [47]. To achieve optimum stability and the best convergence rate in

the time-dependent study, the relative tolerance is set as 10^{-3} for all primary variables and regarded as the convergence criteria of the numerical solutions.

Mathematical model

According to the model presented by Di Donna et al. [34], for negligible soil skeleton deformations (linear kinematics), a saturated medium, and an incompressible fluid and soil particles, the equilibrium equation, conservation of mass, and conservation of energy are written as:

$$\nabla \cdot \sigma_{ij} + \rho g_i = 0 \rightarrow \nabla \cdot \sigma'_{ij} - \nabla u + \rho g_i = 0 \tag{1}$$

$$\partial_t u [(n/K_w) + ((1-n)/K_s)] - \partial_t T [\alpha'] + \nabla \cdot (v_s) + \nabla \cdot (v_{rw,i}) = 0 \tag{2}$$

$$\rho \hat{c} \partial_t T + \nabla \cdot (q) + \rho_w C_{p,w} v_{rw,i} \nabla T = 0 \tag{3}$$

where $\nabla \cdot$ is the divergence operator, ∇ denotes the gradient, σ_{ij} is the total stress tensor, σ'_{ij} is the effective stress tensor, $\rho = n\rho_w + (1-n)\rho_s$ represents the bulk density of the porous material (based on water density ρ_w and solid particle density ρ_s at porosity n), u is pore water pressure, g_i is the gravity vector, ∂_t denotes the time derivative, $1/K_w$ is water compressibility, $1/K_s$ is solid particle compressibility, T is the temperature, $\alpha' = n\alpha'_w + (1-n)\alpha'_s$ denotes the thermal expansion coefficient of the porous material (based on water thermal expansion coefficient α'_w and solid particle thermal expansion coefficient α'_s), v_s is the solid particle velocity, $v_{rw,i}$ is the water velocity relative to solid particles, $\rho \hat{c} = n\rho_w c_{p,w} + (1-n)\rho_s c_{p,s}$ is the bulk heat capacity of the porous material (based on the specific heat capacity of water $c_{p,w}$ and that of solid particles $c_{p,s}$), and q denotes heat flux.

To complete the formulation, it is required to introduce constitutive equations for pore water flux, heat flux, and material behavior. The velocity of water relative to solid particles can be written based on Darcy's law as:

$$v_{rw,i} = -(k/(\rho_w g)) \cdot \nabla (u + \rho_w g z) \tag{4}$$

where k is hydraulic conductivity, and z denotes the vertical coordinate. Here, k is defined as a function of water parameters and intrinsic permeability k^{int} as:

$$k = (k^{int} \rho_w g) / \mu_w \tag{5}$$

where μ_w is water dynamic viscosity. The temperature dependence of k is represented by the temperature dependence of μ_w and ρ_w :

$$\mu_w = 0.6612 \cdot (T - 229)^{-1.562} \tag{6}$$

$$\rho_w = 838.5 + 1.40T - 0.003T^2 + 3.72e^{-7}T^3 \tag{7}$$

where μ_w is measured in Pa.s, and T is measured in K. Fourier's law of heat conduction is assumed to be valid. Then, heat flux is written as:

$$q = -\lambda \nabla T \tag{8}$$

where $\lambda = n\lambda_w + (1-n)\lambda_s$ is the thermal conductivity of the porous material (based on water conductivity λ_w and solid particle conductivity λ_s).

Material behavior under external loading is an important aspect of the system response. Although reinforced concrete was assumed to be thermoelastic, the soil is simulated using a thermoelastic-plastic constitutive model based on the Drucker–Prager failure criterion. The elastic and post-yield effective stress increments are given by:

$$d\sigma'_{ij} = C_{ijkl} (d\epsilon_{kl}^e - \alpha'_s I_{kl} dT) \tag{9}$$

$$d\sigma'_{ij} = C_{ijkl} (d\epsilon_{kl} - d\epsilon_{kl}^p - \alpha'_s I_{kl} dT) \tag{10}$$

where $d\epsilon_{kl}$ is the total strain increment, $d\epsilon_{kl}^e$ is the elastic strain increment, $d\epsilon_{kl}^p$ is the plastic strain increment, I_{kl} is the Cauchy stress tensor, and C_{ijkl} denotes the fourth-order stiffness tensor, which consists of Young's modulus E and Poisson's ratio ν in an isotropic system. The plastic strain increment of the soil can be described using the flow rule:

$$d\epsilon_{ij}^p = \lambda_p \left(\partial g / \partial \sigma'_{ij} \right) \tag{11}$$

where λ_p is the plastic multiplier, while g denotes the plastic potential surface. This model assumes the plastic potential surface to be similar to the yield surface (with a size based on the Mohr–Coulomb criterion). However, the effective friction angle is replaced with the effective dilation angle ψ' , and the flow rule becomes non-associated due to their different values.

For stiff clays exposed to limited temperature changes, the assumption of thermoelastic response is acceptable as an initial approximation of the soil behavior [36]. But for soft clays, the temperature changes under non-isothermal conditions affect the size of the yield surface [32], and thus this model is not applicable.

It should also be noted that cyclic loading produced by the thermal operation of the system may lead to quick clay conditions and disastrous failure [48]. However, soils with low to medium plasticity and stiff over-consolidated clays tend to be insensitive [49], so strength loss does not occur in the considered problem.

This study adopted the solid mechanics' sign convention of stresses, strains, and pore water pressure.

Therefore, stress and strains are positive under tension, while pore water pressure is positive under compression.

System geometry

Similar to the study conducted by Salciarini et al. [36], the design of a large-scale piled raft foundation in stiff saturated clay was used. The foundation had a raft with a thickness of 0.8 m on concrete piles with a diameter of $D = 1$ m, a length of $L = 25$ m, and a center-to-center spacing of $S = 2D$. Due to the symmetry of the system geometry and external loading, modeling can be carried out on a unit cell of the system with a depth of $2L$, as shown in Fig. 1. It is worth noting that this unit cell in modeling represents the worst-case scenario for changes in axial load and settlement. Unlike the assumption of rigid boundaries and uniform strain in the unit cell, outer piles at foundations are free to bend outward due to less confining stress with lateral displacement of the soil, leading to a more conservative estimation of group effects in the unit cell.

The domain was discretized using tetrahedral elements through quadratic interpolation for displacements and pore water pressure and linear interpolation for the temperature. The discretization of the model, which was controlled using sensitivity analysis to avoid undesirable conditions, led to a grid with 54,368 elements and a total of 384,532 degrees of freedom.

Initial and boundary conditions

The initial conditions included the initial stress, groundwater level, and initial temperature in the domains. Due to gravity, the initial stress was assumed to be geostatic; i.e., the weights of the model components were applied before loading. For a water table at the underlying raft level, hydrostatic conditions were applied to the initial pore water pressure distribution. However, it should be

noted that the groundwater table pattern can be affected by geo-engineering projects in combination with changes in climate and natural variability. Therefore, despite the assumption of constant water level, an uncertainty quantification analysis can be performed to account for this nonlinear time-dependent concern [50]. Furthermore, the ground temperature at shallow depths is dependent on ambient temperature [51], which indicates the necessity of considering temperature variations in these areas and applying them as the initial temperature. The ground temperature at depth z and time t can be formulated as [52]:

$$T(z, t) = T_m + A_0 \exp\left(-z\sqrt{\pi/(\alpha_u p)}\right) \times \sin\left((2\pi/p)t - z\sqrt{\pi/(\alpha_u p)}\right) \quad (12)$$

where T_m is the average soil temperature, A_0 is the temperature amplitude on the ground surface, α_u is the thermal diffusivity of the soil, and p denotes the period. This study assumed T_m and A_0 to be 18 °C and 9 °C, respectively, and p to be 1 year. Here, α_u is a measure to show how rapidly the soil responds to temperature changes. It is defined as [52]:

$$\alpha_u = \lambda/(\rho\hat{c}) \quad (13)$$

The boundary conditions included displacements, groundwater flow, heat flux, interaction, and thermomechanical loads. For stiff bedrock under the soil layer, fixed displacements, zero heat flux, and zero groundwater flow were applied to the end of the model. It should be noted that this boundary was assumed to be deep enough to neutralize possible boundary effects on the system response. Furthermore, in the vertical planes of symmetry, the normal component of the displacement vector was fixed, and no heat flux and groundwater flow existed.

A fine mesh was used near the soil-structure interface to avoid stress localization, where relatively large shear forces were expected, and the coarser mesh was adopted further away from the structure. However, the elements distribution was optimized using a convergence study that ensured sufficient accuracy and minimized computational time and resources. The soil-structure interface was simulated using contact modeling. The penalty contact algorithm was adopted, in which contact pressure would be calculated using the normal and tangent penalty factors (p_n and p_t , respectively) as the stiffness of springs connecting the contact boundaries. These factors represent interface stiffness and measure boundary penetration in the normal direction and relative surface sliding in the tangent direction [47].

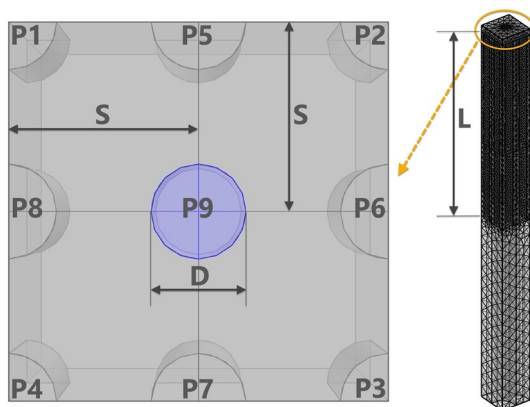


Fig. 1 The geometric layout of the piled raft foundation

The Coulomb model was employed to reflect friction between the side surfaces of the piles and surrounding soil. The tangent load T_t is defined as [47]:

$$T_t = \mu T_n + T_{\text{Coh}} \tag{14}$$

where T_n is the normal load, μ is the friction coefficient, and T_{Coh} denotes cohesion sliding resistance. The friction coefficient μ is obtained based on the following equation [53]:

$$\mu = \tan(\delta') \tag{15}$$

where δ' is the interface friction angle. The magnitude δ' is assumed to be equal to $0.7 \varphi'$ [53].

The strength of structural interfaces with fine-grained soils under non-isothermal conditions exhibits a slight sensitivity to temperature variations. This evidence is related to the more pronounced sensitivity of fine-grained soils to temperature variations compared to coarse-grained soils, both in terms of volumetric and deviatoric behavior [4]. However, the studied clay is considered to be stiff enough so that the plastic yielding effects and softening caused by thermal deformations are negligible.

To simulate the transferred mechanical load of the superstructure in the first loading stage, a vertical concentrated load was applied in the center of the unit cell. In the second step of loading, which was considered for 20 years without daily temperature variation, a uniform thermal load that changed under a sinusoidal pattern over time was applied to the energy pile body. The temporal evolution of the energy pile temperature generally includes a period of several months associated with seasonal temperature changes and alternation in the phases of the air conditioning system, which its profile can be assumed uniform with depth based on the measurements derived

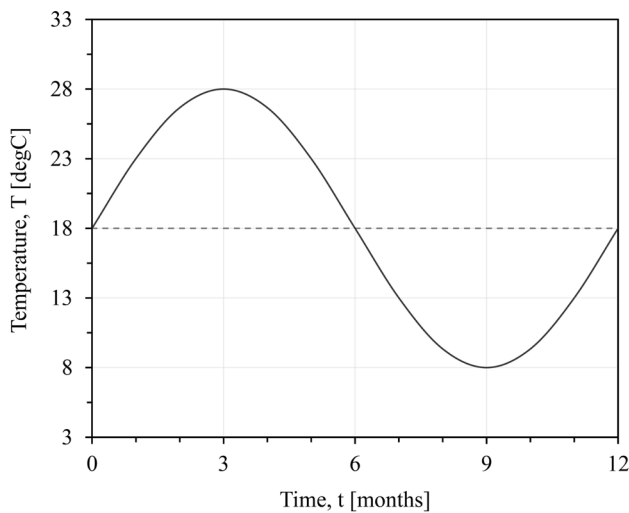


Fig. 2 The energy pile temperature during the thermal loading

from the pile tests [51, 54]. In this transient thermal load representing normal geothermal heat pump operation with a period of one year, the average temperature and thermal load amplitude were set to 18 °C and 10 °C, respectively, as shown in Fig. 2.

Simulation program

The numerical model scheme was validated at first using full-scale in situ tests. Then, parametric analysis was carried out by changing interface stiffness and mechanical loads in a system consisting of active and passive piles (representing thermal piles connected to the heat transfer system and conventional piles without additional inner pipes, respectively), as shown in Fig. 1. Tables 1 and 2 report the material properties and numerical parameters, respectively [32, 34, 53, 55–60]. One of the practical difficulties of the method used is the non-commonness of required tests for measuring

Table 1 The material properties of the piled raft foundation [32, 34, 53, 55–60]

Property	Unit	Soil	Piles	Raft
E	MPa	50	2.20e4	2.20e4
ν	–	0.25	0.25	0.25
ρ_s	kg/m ³	2613	2667	2667
ρ_w	kg/m ³	Equation (7)	Equation (7)	Equation (7)
n	–	0.38	0.10	0.10
φ'	°	25	–	–
c'	kPa	15	–	–
ψ'	°	7.50	–	–
α'_s	1/K	2.26e–5	1.00e–5	1.00e–5
α'_w	1/K	2.00e–4	2.00e–4	2.00e–4
λ_s	W/mK	1.89	1.93	1.93
λ_w	W/mK	0.60	0.60	0.60
$c_{p,s}$	J/kgK	2722	742	742
$c_{p,w}$	J/kgK	4186	4186	4186
k	m/s	1.00e–9	2.00e–10	2.00e–10
μ	–	0.315	–	–

Table 2 The variable parameters in the numerical modeling

Analysis	Soil-structure p_n [N/m ³]	Soil-structure p_t [N/m ³]	Pile-raft p_n [N/m ³]	Mechanical load [N]
B1	1.5e7	6.0e6	1.0e9	1250e3
B2	1.0e7	4.0e6	1.0e9	1250e3
B3	2.0e7	8.0e6	1.0e9	1250e3
B4	1.5e7	6.0e6	5.0e8	1250e3
B5	1.5e7	6.0e6	2.0e9	1250e3
B6	1.5e7	6.0e6	1.0e9	1000e3
B7	1.5e7	6.0e6	1.0e9	1500e3

material thermal properties (such as thermal expansion coefficient, thermal conductivity, and heat capacity). A combination of the results of experimental tests on samples collected on-site and information from studies conducted in the same geographical areas is usually used in these cases.

It is worth noting that soil-structure interface stiffness was assumed to be the same throughout the system, which can be applied to piles in stiff over-consolidated clays.

Validation

The numerical model was validated through comparison to full-scale in situ tests on the foundation of a water reservoir in the Swiss Federal Institute of Technology, Lausanne [16]. The concrete foundation consisted of a raft with a thickness of 0.9 m and an area of $9 \times 25 \text{ m}^2$, four energy piles (EP1, EP2, EP3, and EP4) with a length of 28 m and

a diameter of 0.9 m, and sixteen conventional piles in a fully saturated multilayer soil, as shown in Fig. 3a. To control the THM response of the system, all the energy piles were instrumented with thermocouples, optical fibers, and strain gauges in the longitudinal direction and pressure cells at their heads, while the two soil profiles (meaning two boreholes in the soil, labeled S1 and S2 in Fig. 3a) were equipped with thermistors and piezometers.

The field study involved two independent sets of tests. The tests of the first set were carried out on unconstrained-head piles, while the second set was performed with a fixed load applied to the pile heads to represent post-construction conditions. In the second set, including several independent tests, the energy piles were at first subjected to mechanical loading to reflect the dead load of the superstructure. Then, thermal loads (temperature variations) were separately applied to the pile bodies [16]. As shown in Fig. 3b, EP1 operated as an active pile for 8.75 days in

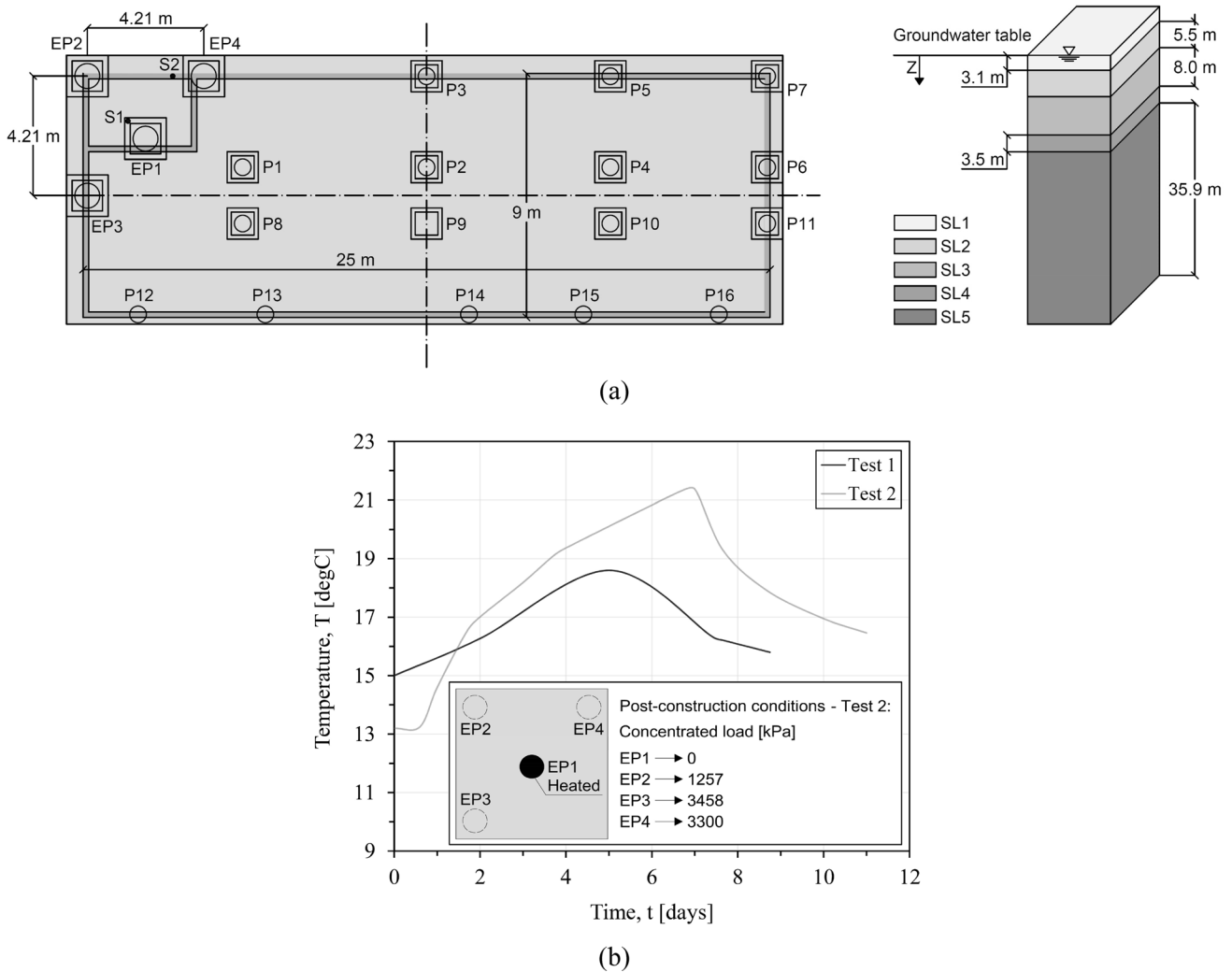


Fig. 3 The full-scale in situ tests in the EPFL [16, 34] a the layout of the problem and b EP1 temperature during the thermal loading

Table 3 The material properties used to simulate the in situ tests performed in EPFL [34]

Property	Unit	Soil layers					Piles	Raft
		SL1	SL2	SL3	SL4	SL5		
E	MPa	190	190	84	90	3000	2.80e4	3.50e4
ν	–	0.22	0.22	0.40	0.40	0.30	0.25	0.25
ρ_s	kg/m ³	2769	2769	2735	2740	2556	2667	2667
ρ_w	kg/m ³	1000	1000	1000	1000	1000	1000	1000
n	–	0.10	0.10	0.35	0.30	0.10	0.10	0.10
φ'	°	30	27	23	27	35	–	–
c'	kPa	5	3	6	20	2000	–	–
ψ'	°	7.50	7.50	7.50	7.50	7.50	–	–
α'_s	1/K	1.00e–5	1.00e–5	1.00e–4	1.00e–4	1.00e–6	3.00e–5	3.00e–5
α'_w	1/K	2.00e–4	2.00e–4	2.00e–4	2.00e–4	2.00e–4	2.00e–4	2.00e–4
λ_s	W/mK	3.38	3.38	4.45	4.17	3.38	1.63	1.63
λ_w	W/mK	0.60	0.60	0.60	0.60	0.60	0.60	0.60
$c_{p,s}$	J/kgK	880	880	890	890	923	837	837
$c_{p,w}$	J/kgK	4186	4186	4186	4186	4186	4186	4186
k	m/s	7.00e–6	1.00e–5	1.00e–5	2.00e–10	2.00e–10	2.00e–10	2.00e–10
μ	–	0.346	0.335	0.289	0.342	0.456	–	–

the first set of tests and 11 days in one test of the second set, which was simulated to validate the numerical modeling [34]. Table 3 represents the mechanical, thermal, and hydraulic parameters of the piles, raft, and soil layers.

Figure 4 compares the experimental and numerical axial stresses at the end of the heating and vertical displacement in EP1. As can be seen, the model effectively reproduced the field data, which verifies the efficiency of the numerical approach and reliability of the modeling. However, due

to the high variability of soil properties in practice and the intrinsic errors of numerical modeling, absolute magnitudes differ somewhat. The difference between the numerical and experimental results was quantified as:

$$R_d = ((X_n - X_f)/X_f) \times 100 \tag{16}$$

where X_n and X_f denote the numerical and field parameter values of EP1, respectively.

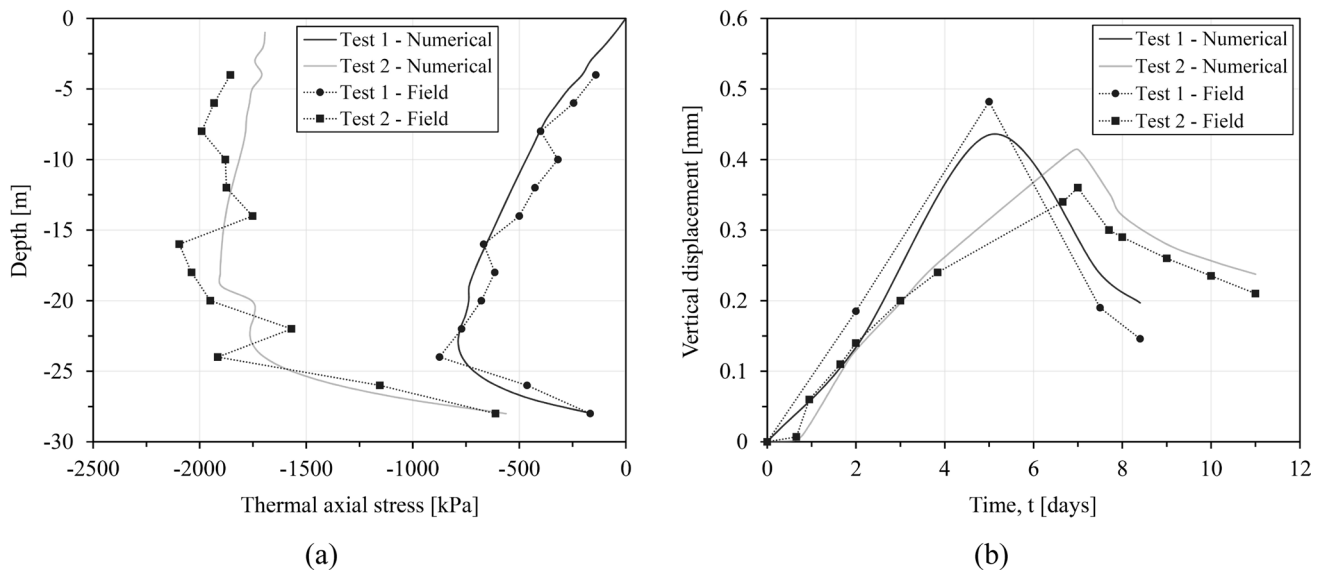


Fig. 4 A comparison of the experimental [16] and numerical results for EP1 **a** the thermal axial stress variations at the end of the heating and **b** the vertical displacement variations during the thermal loading

Table 4 A quantitative comparison of the experimental and numerical results for EPI

Characteristic	Unit	X_r		X_n		R_d [%]	
		Test 1	Test2	Test 1	Test 2	Test 1	Test 2
Max. thermal axial stress	kPa	-874	-2096	-787	-1903	-9.95	-9.21
Max. thermal vertical displacement	mm	+0.48	+0.36	+0.43	+0.41	-10.42	+13.89

As presented in Table 4, for the maximum thermal axial stress and vertical displacement, R_d was calculated to be -9.95% and -10.42% for the unconstrained-head pile (Test 1) and -9.21% and +13.89% for the post-construction conditions (Test 2), respectively. This suggests a generally good agreement between the numerical and experimental results.

Results and discussion

This section provides the numerical simulation results to evaluate the mechanical fields of the energy pile foundation under different interface constraints. The thermal operation of energy piles poses THM effects on the responses of the system. This is evaluated with a focus on spatial and temporal evolutions in terms of:

- Axial stresses of the piles
- Mobilized soil-pile interface stresses
- Vertical raft displacement, and
- Load distribution between the piles and soil-raft interface.

The parameters were undimensionalized using the normalized pile thermal axial stress $N_{\Delta\sigma}$, shaft thermal shear stress $N_{\Delta\tau_s}$, pile base thermal contact stress $N_{\Delta\sigma_b}$, thermal vertical displacement in the middle of the top surface of the raft $N_{\Delta w}$, and depth N_d were used:

$$N_{\Delta\sigma} = ((\sigma_t - \sigma_0) / \sigma_0) \times 100 \tag{17}$$

$$N_{\Delta\tau_s} = ((\tau_{s-t} - \tau_{s-0}) / \tau_{s-0}) \times 100 \tag{18}$$

$$N_{\Delta\sigma_b} = ((\sigma_{b-t} - \sigma_{b-0}) / \sigma_{b-0}) \times 100 \tag{19}$$

$$N_{\Delta w} = ((w_t - w_0) / w_0) \times 100 \tag{20}$$

$$N_d = d_z / L \tag{21}$$

where σ_t is the axial stress of the pile at time t , σ_0 is the initial axial stress of the pile (under the mechanical load with no thermal loading), τ_{s-t} is the shaft shear stress at time t , τ_{s-0} is the initial shear stress of the shaft, σ_{b-t} is the contact stress of the pile base at time t , σ_{b-0} is the initial pile base

contact stress, w_t is the vertical displacement of the raft at time t , w_0 is the initial vertical raft displacement, and d_z denotes the selected depth.

Axial stress of the piles

Figure 5 depicts the pushover curve of the normalized pile thermal axial stress $N_{\Delta\sigma}$ at different depths for B1. Due to the symmetry of the system, the corner piles had the same load, as well as the piles on the four sides. Therefore, only P9, P5, and P1 are analyzed.

As can be seen, the axial stress variation was substantially larger at shallow areas than at deep areas, which is qualitatively consistent with the observations of the energy pile foundation by Mimouni and Laloui [16]. In fact, the tendency of piles to undergo thermal deformation induces a reaction in the pile-raft connection, leading to large thermal stresses near the pile head, which are larger than the thermal stresses of other areas. This occurs both in active P9 and passive P1 and P5, with the difference that these piles experience opposite changes in the axial stress to meet static equilibrium. In heating cycles, active P9 undergoes thermal expansion, leading to a rise in the axial stress due to the constrained deformation. P1 and P5, however, tend to undergo compression upon the upward vertical displacement of the raft, experiencing an axial stress reduction. The opposite is the case with cooling; i.e., active P9 experiences thermal contraction and axial stress reduction, while the downward vertical raft displacement increases the axial stresses of passive P1 and P5. Thus, the constraint imposed by the raft and the surrounding soil can be assumed to be a key determinant of axial stresses in the piles.

Figure 6 plots the thermal axial stress variation range of the piles. To assess the intended range, $|\Delta N_{\Delta\sigma}|$ is defined as:

$$|\Delta N_{\Delta\sigma}| = |[N_{\Delta\sigma}]_{\max} - [N_{\Delta\sigma}]_{\min}| \tag{22}$$

where $[N_{\Delta\sigma}]_{\max}$ and $[N_{\Delta\sigma}]_{\min}$ denote the maximum and minimum normalized thermal axial stresses of the pile in a certain loading cycle, respectively. Since $|\Delta N_{\Delta\sigma}|$ was the same at different times (see Fig. 5), the variation range associated with the 11th cycle is evaluated.

A change in the constraints expectedly changed the thermal stresses of the piles. Based on the curves, higher soil stiffness (B3), a stronger connection (B5), and a smaller mechanical load (B6) led to a larger $|\Delta N_{\Delta\sigma}|$, while lower

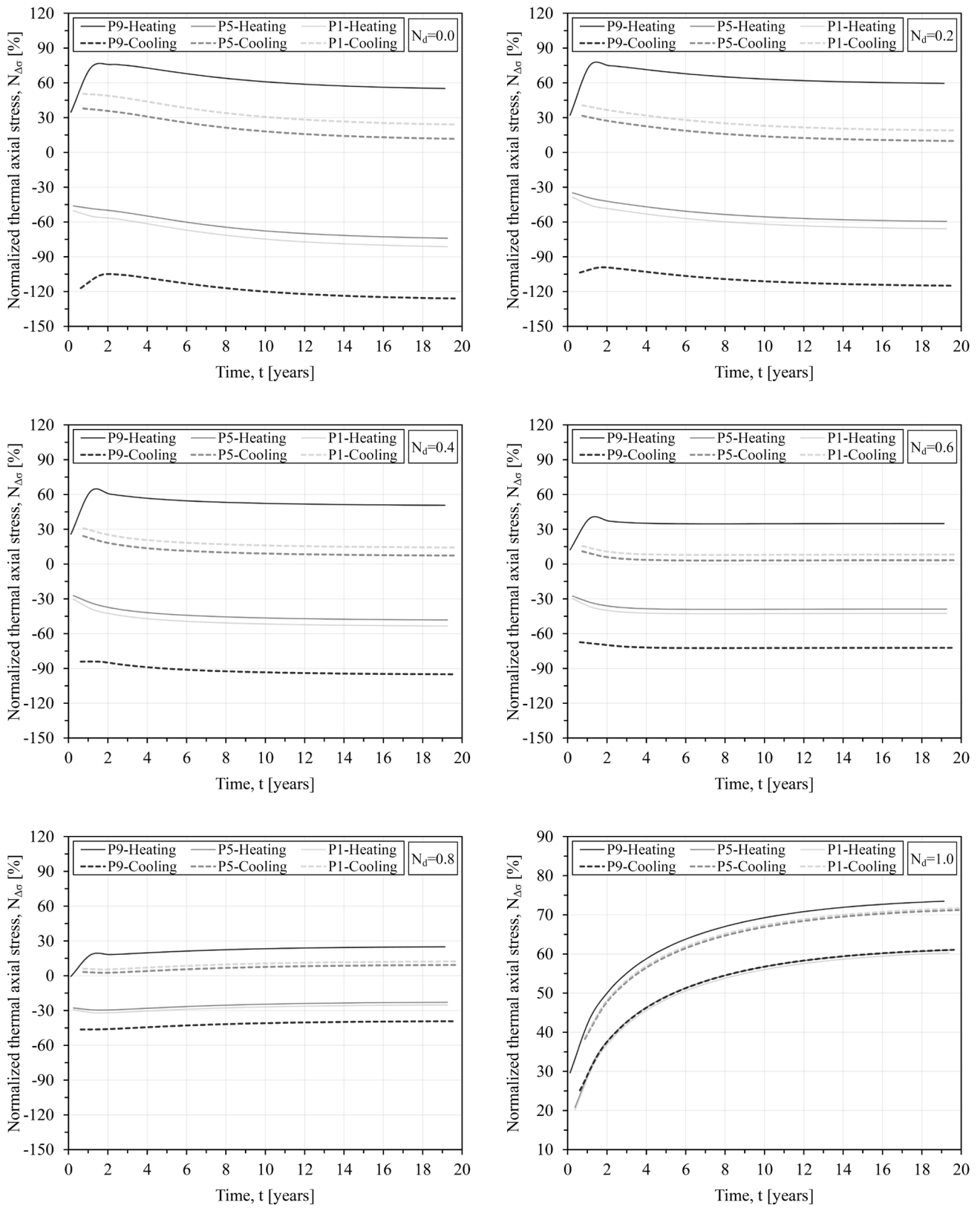


Fig. 5 The pushover curve of the thermal axial stress at different depths for B1

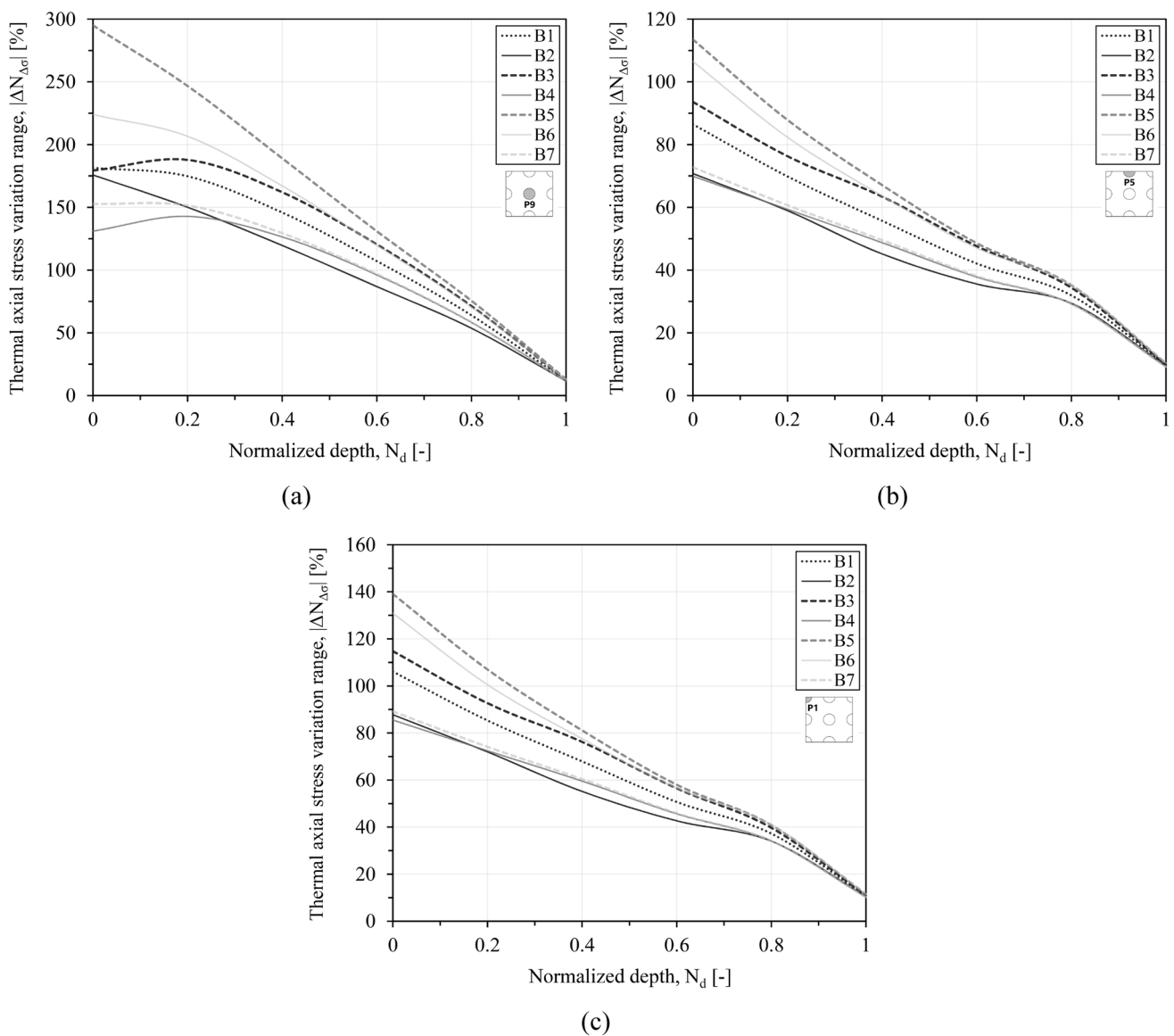


Fig. 6 The thermal axial stress variation range of the piles **a** P9; **b** P5; and **c** P1

soil stiffness (B2), a weaker connection (B4), and a larger mechanical load (B7) resulted in a smaller $|\Delta N_{\Delta\sigma}|$. As the magnitude of the excess axial stress is a function of pile degree of freedom, $|\Delta N_{\Delta\sigma}|$ could be studied by evaluating the displacements of the system components and piles constraining.

An increase in soil stiffness increases the friction strength of the pile shaft and reduces the load-sharing ratio of the piles, leading to relatively the same axial stress profile in the piles before thermal loading. Thus, the thermal/mechanical axial stress ratio increases due to a further thermal deformation constraint. Likewise, a rise in the stiffness of the pile-raft connection raises the reactive stresses, with the piles resisting larger excess loads upon a change in the temperature. However, it was observed that a larger mechanical

load on the foundation had a different effect; i.e., the further constraint caused by it did not raise $|\Delta N_{\Delta\sigma}|$ compared to a smaller mechanical load. This does not necessarily suggest an increase in the thermal axial stress under a smaller mechanical load; rather it implies that the magnitude of the mechanical axial stress is a determinant of $N_{\Delta\sigma}$. In other words, the thermal axial stress magnitude under practical operations is not dependent on the initial stresses, and a larger initial pile axial stress would lead to a larger reduction in $|\Delta N_{\Delta\sigma}|$.

Furthermore, the axial stress changes mostly occur at shallow depths, and the variation range magnitude at the pile ends is the same, regardless of the constraint. To explain this behavior, it is required to understand the function of floating piles, which resist loads mostly through shaft friction and

have lower base capacity importance than end-bearing piles. As the raft and mechanical load along with shaft strength pose a greater constraining effect than the base strength in such foundations, the pile end stresses undergo smaller changes, leading to smaller thermal axial stress variations. In the most critical cases, the maximum and minimum thermal axial stress variation range of P9 were found to be 294.93% and 11.36% of the mechanical axial stress, respectively (as shown in Fig. 6a). This implies that excess stresses should be incorporated into the structural design of piles.

Previous evidence shows that the effects of thermal loads generally do not cause the failure of energy piles and only significantly characterize the deformation of these piles. In terms of the reinforced concrete performance, heating thermal loads usually cannot overcome compressive strength, and conversely, cooling thermal loads should be considered as critical variables in the performance-based design of energy piles [61].

It should also be noted that since geological materials are formed under a wide variety of complex physical conditions, the history of which is not completely known, geomechanics involves many uncertainties. In dealing with these uncertainties, a logical step beyond the numerical approach is to use capacity design principles. In the basic form of capacity design, there are two types of design methods: Allowable Stress Design (ASD) and Load and Resistance Factor Design (LRFD). In many parts of the world, ASD and LRFD are also known as working stress design and limit-state design, respectively. ASD compares capacities derived from the allowable stress against the service loads without any load factors, while limit-state design has factors for loadings and partial factors for materials. When either of them is used, it greatly reduces the uncertainty of loads and material properties, simplifying the task of creating a reliable analysis model [62].

Mobilized stresses in the soil-pile interface

From a geotechnical perspective, the cyclic thermal expansion and contraction of piles not only affect the axial stress distribution but also challenge the mobilized stresses in the soil-pile interface. Figure 7 plots the shaft shear stress versus the base contact stress during the thermal loading for active P9 under different conditions.

Once head-constrained piles undergo a temperature variation, the total mobilized strength along the pile shaft and base changes, being no longer equal to the mechanical load in the first loading stage. As can be seen, the curves have a common implication; repetitive stress reversals substantially influence the magnitude of strengths in long-term operations, so that the pile shaft shear stress declines over time due to the softening behavior of the soil-pile interface, reducing the axial stress of the pile upper part. However, due

to the partial constraint, the pile base remains stable with an increase in the contact stress, increasing the axial stress of the pile tip (see Fig. 5). Nevertheless, it is obvious that the constraining factors have different effects on mobilized strengths.

The pile expands upon a temperature rise, and bearing stress rises due to the downward displacement of the pile base. On the other hand, a temperature reduction leads to pile contraction, with the bearing stress reducing due to the upward displacement of the base. However, the shear stress is dependent on the stress path in the soil-pile interface and axial displacement in the longitudinal direction. Overall, the pile nodes upward/downward displacement relative to the soil nodes reduces/increases the shear stresses of the soil-pile interaction. Therefore, the location of the null-point along the pile (at which stress reversal from negative to positive occurs) and interface constraint conditions can be assumed as the major mobilized strength determinants of the shaft.

According to Fig. 7a, a rise in the soil stiffness increased/reduced the normalized thermal shear stresses of the pile shaft in heating/cooling cycles. Once soil stiffness increases, the thermal longitudinal deformation constraint increases and downshifts the null-point; i.e., the length of those parts of the pile that relative to the soil moves downwards during heating cycles and upwards during cooling cycles will decrease in stiffer soil. However, a stiffer interface with higher continuity leads to a larger tangential force in the pile shaft and increases shear stresses arising from a temperature change. As can be seen, the resultant of these two contradictory effects increases the shaft strength variation range in stiffer soils. It should be noted that stiffer soil reduces the shaft strength diminution rate over thermal loading cycles, which means reducing softening behavior in the soil-pile interface. This increases/decreases the normalized thermal shear stress magnitude difference between the stiffer soil (B3) and softer soil (B2) at the end of the 20th cycle under heating/cooling modes. Furthermore, a soil stiffness reduction increases pile base expansion, raising the contact stress in heating cycles, while pile base contraction is not significantly dependent on soil stiffness (due to the negligence of the tensile strength of the soil). Thus, the contact stress declines in cooling cycles. Accordingly, it can be said that soil stiffness reduction always increases the thermal contact stresses of the pile base.

Figure 7b illustrates the effect of pile-raft connection stiffness on the strengths. A rise in pile-raft connection stiffness enhances pile-raft continuity, raising the pile head constraint. This reduces the degree of freedom of thermal deformations near the pile head, upshifting the null-point and increasing the shaft strength variation range; i.e., the thermal shear stresses increase in heating cycles and reduce in cooling cycles. However, it was observed that the contact

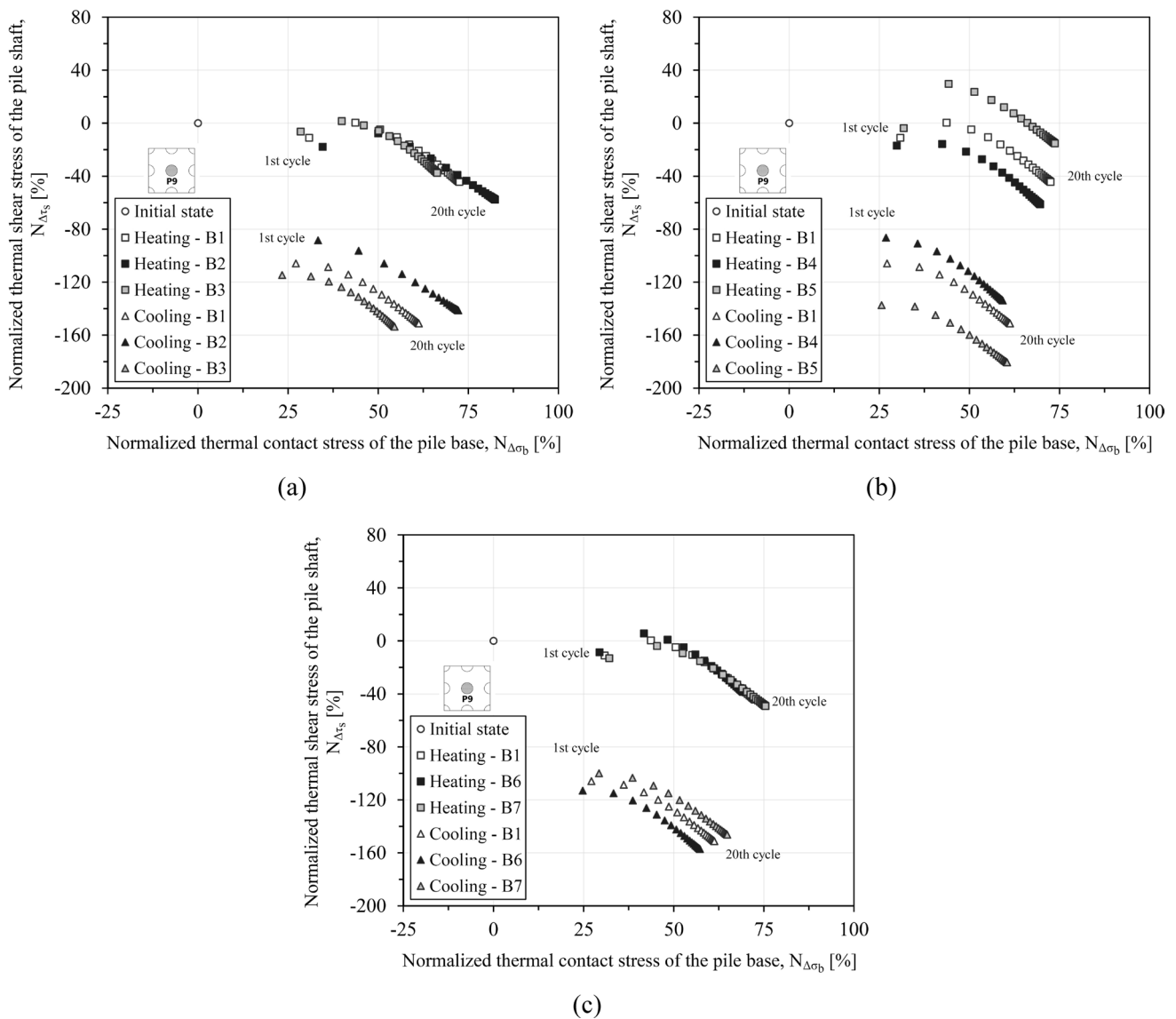


Fig. 7 The shaft thermal shear stress versus the base thermal contact stress for P9 **a** B1–B2–B3; **b** B1–B4–B5; and **c** B1–B6–B7

stresses of the pile base did not change substantially. This suggests that the compactness of the soil below the pile is not heavily dependent on pile-raft connection stiffness. In fact, the reactive stress change of the pile head (due to the change in connection stiffness) is mostly neutralized by the change in shaft strength.

Figure 7c plots the mechanical load effect on the strengths. As can be seen, the normalized thermal shear stresses were almost the same in heating cycles; however, their difference was larger in cooling cycles, which could be attributed to the pile displacement. An increase in the mechanical load under a given thermal load reduces the net upward displacement of the pile body in heating cycles and increases its downward displacement in cooling cycles. This increased/reduces the relative displacements of pile

and soil nodes in heating and cooling cycles, respectively. As a result, larger positive shear stresses appear in heating cycles, and smaller negative shear stresses occur in cooling cycles. In addition, a rise in the mechanical load raises the normal stress in the soil-pile interface, increasing the initial shear stress. Hence, based on the formulation of $N_{\Delta\tau_s}$, the curves move closer in heating cycles and distant in cooling cycles. As with the pile body, an increased mechanical load increases the pile base expansion in heating cycles and reduces the pile base contraction in cooling cycles, leading to higher stress enhancement and lower stress relaxation in the contact area, respectively. Therefore, the mobilized contact stress of the pile base increases with the increase of the mechanical load.

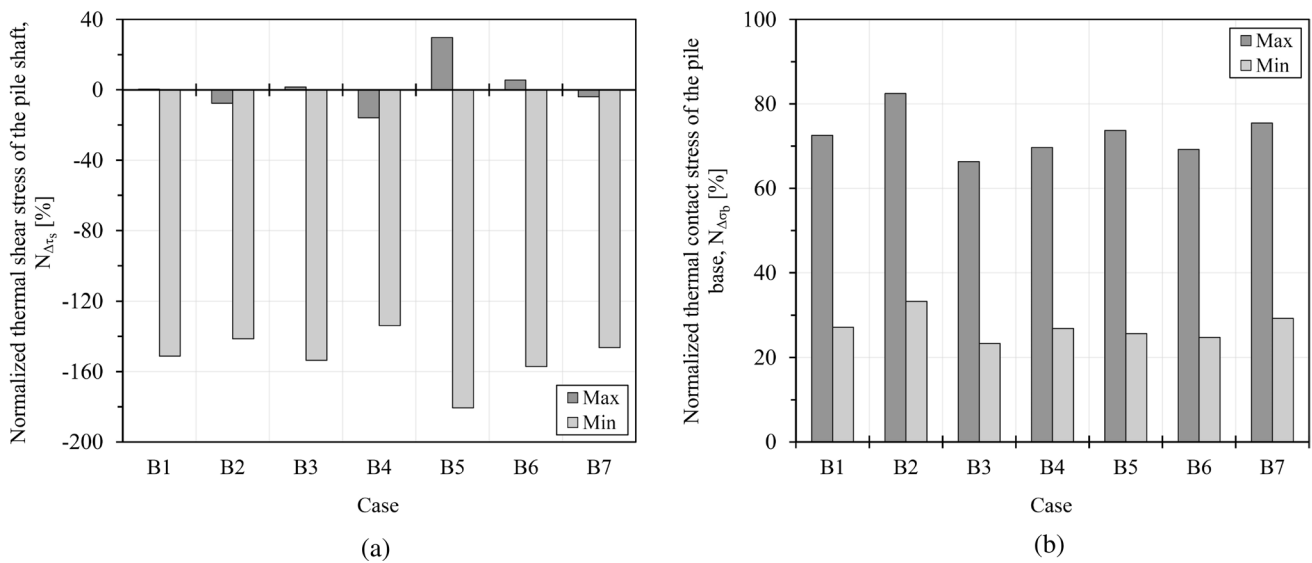


Fig. 8 The extrema of the normalized stresses under different conditions for P9 **a** the shaft thermal shear stress and **b** the base thermal contact stress

Figure 8 plots the extrema of $N_{\Delta\tau_s}$ and $N_{\Delta\sigma_b}$ under different conditions. As can be seen, the minimum and maximum $N_{\Delta\tau_s}$ values were +29.68% (B5) and -180.65% (B5), respectively, while the maximum and minimum $N_{\Delta\sigma_b}$ values were obtained to be +82.43% (B2) and +23.34% (B3), respectively.

Vertical displacement of the raft

Figure 9 indicates the normalized thermal vertical displacement pushover curve in the middle of the top surface of the

raft $N_{\Delta w}$ under different conditions. The heating of the soil around active P9 led to the partial uplift and reduced vertical displacement of the raft, while the opposite is the case with cooling. However, it was observed that the vertical displacement of the raft increased over time, approaching a stabilized excess settlement.

According to Fig. 9a, a change in soil stiffness strongly changes the vertical displacement of the raft in heating cycles, while changes in connection stiffness and mechanical load had no significant effects. This can be explained by the larger thermal expansion coefficient of the saturated soil

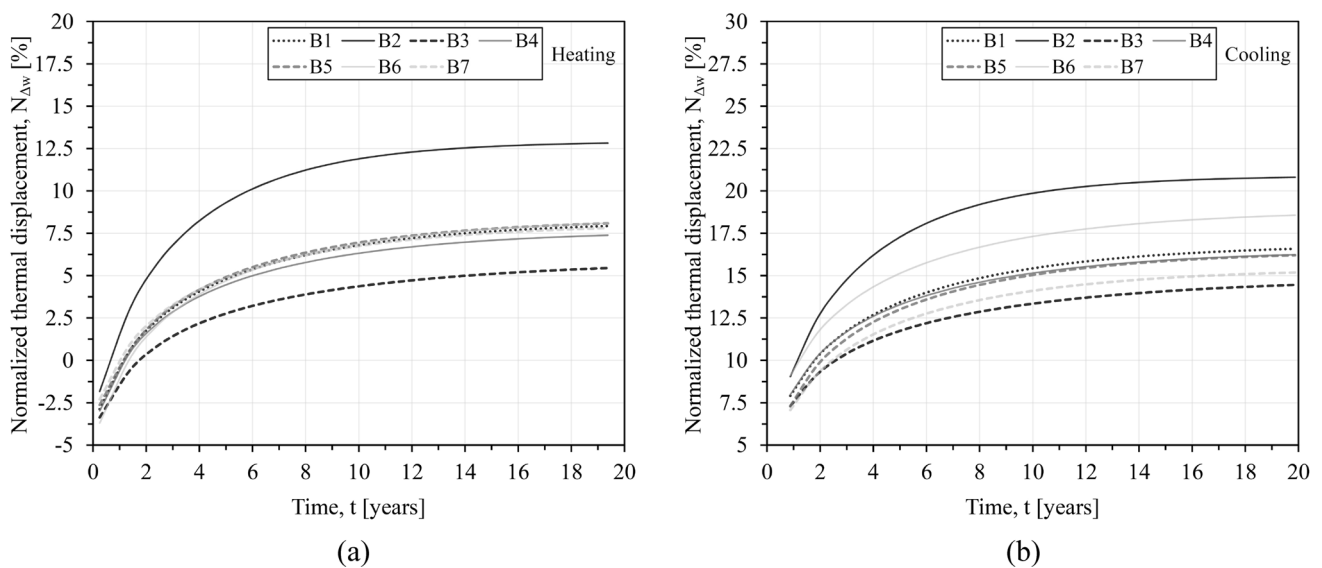


Fig. 9 The pushover curve of the thermal vertical displacement in the middle of the top surface of the raft **a** heating cycles and **b** cooling cycles

than the piles. Since soil tends to undergo a larger expansion than the piles, soil-raft interface stiffness becomes a vertical displacement determinant of the raft under a given thermal load; an increase/reduction in the stiffness of the connecting springs increases/reduces the upward displacement of the raft.

According to Fig. 9b, only connection stiffness is a non-influential parameter in cooling cycles. As can be seen, softer soil (B2) and a smaller mechanical load (B6) raised the normalized downward displacement of the raft, whereas stiffer soil (B3) and a larger mechanical load (B7) decreased it. A soil with lower stiffness has higher pile contraction-induced penetration, leading to a larger raft settlement. As mentioned, a reduction in the mechanical load has two different effects on pile displacement in cooling cycles; it reduces the downward displacement in the top part of the pile and increases the upward displacement in the bottom part of the pile. However, as the soil undergoes greater contraction than the pile and the raft experiences a smaller initial settlement, $N_{\Delta w}$ is larger under a smaller mechanical load. It should be noted that the similarity of the curves for the mechanical load in heating cycles suggests a combination of a larger net settlement and a smaller upward displacement under a larger mechanical load and a smaller net settlement and a larger upward displacement under a smaller mechanical load, leading to almost the same normalized vertical displacement (based on the formulation of $N_{\Delta w}$).

The evaluation of the stabilized ultimate displacement demonstrates that the maximum and minimum thermal raft displacements at the end of the thermal loading were +12.82% (B2) and +5.45% (B3) of the mechanical vertical displacement in heating cycles and +20.8% (B2) and +14.45% (B3) of the mechanical vertical displacement in cooling cycles, respectively (as shown in Fig. 9).

Load distribution between the piles and soil-raft interface

To obtain deeper insights into the effects of the thermal load on the system, Fig. 10 plots the temporal evolution of the resultant load transferred to the soil-raft interface and pile heads. To calculate the resultant load transferred, the load-sharing ratio is defined as:

$$R_{l-sh} = L_x/L_t \quad (23)$$

where L_x is the resultant load transferred to the soil-raft interface or pile heads, while L_t is the total load transferred.

Due to the raft-induced constraint, the tendency of the soil to undergo larger thermal deformations than the piles leads to larger/smaller contact stresses in the soil-raft interface in heating/cooling cycles. These changes in the load shares should be neutralized by the piles (for static

equilibrium). Hence, the resultant load transferred to the pile heads experiences the opposite evolution. As with the temporal evolutions of the pile axial stresses and vertical raft displacement, it was observed that an increase in the thermal loading cycles led to a smaller increase rate of the resultant load transferred to the soil-raft interface and a smaller reduction rate of the resultant load transferred to the pile heads, approaching a stabilized value.

As can be seen, a change in soil stiffness and mechanical load substantially changed the load-sharing ratio, whereas a change in connection stiffness had no significant effect during thermal loading. In general, lower soil stiffness results leads in a larger load-sharing ratio of the soil-raft interface under thermal loading; however, it reduces the load-sharing ratio of the soil-raft interface in initial heating cycles, which can be attributed to the higher compaction of softer soil in loading cycles due to the increased penetration of the raft into the soil. The level of initial involvement of the raft in the softer soil is not large enough to increase the resulting contact stress above that of the stiffer soil; however, upon alternating thermal deformations, the settlement of the softer soil increases further, leading to a larger load-sharing ratio in heating and cooling cycles. Nevertheless, once the raft has penetrated the soil up to a certain depth (depending on the stiffness coefficient of the connecting springs), the remaining load is transferred to the piles. Therefore, a larger mechanical load would increase the load-sharing ratio of the pile heads and reduce that of the soil-raft interface. This is particularly the case with heating cycles since the contact stress of the soil reduces in cooling cycles due to the larger contraction of soil than piles, with the majority of the load being transferred to the pile heads anyway. Moreover, since pile-raft connection stiffness is much higher than soil-raft interface stiffness, a change in the stiffness of the connection would not significantly change the load-sharing ratio. It should be noted that a stronger connection maximizes the load-sharing ratio of the pile heads in initial cooling cycles (despite an insignificant difference with the other cases).

Figure 11 depicts the limit states of the load distribution between the system components, representing the minimum and maximum load-sharing ratios of the pile heads and soil-raft interface. As can be seen, the most critical load-sharing ratio in the soil-raft interface and pile heads was calculated to be 0.72 and 0.28 (B2) in heating cycles and 0.083 and 0.917 (B5) in cooling cycles, respectively.

Conclusion

The primary objective of the present study was to obtain deeper insights into the behavior of energy pile foundations under different constraints. To this end, a set of coupled THM simulations were run via FE modeling to evaluate the

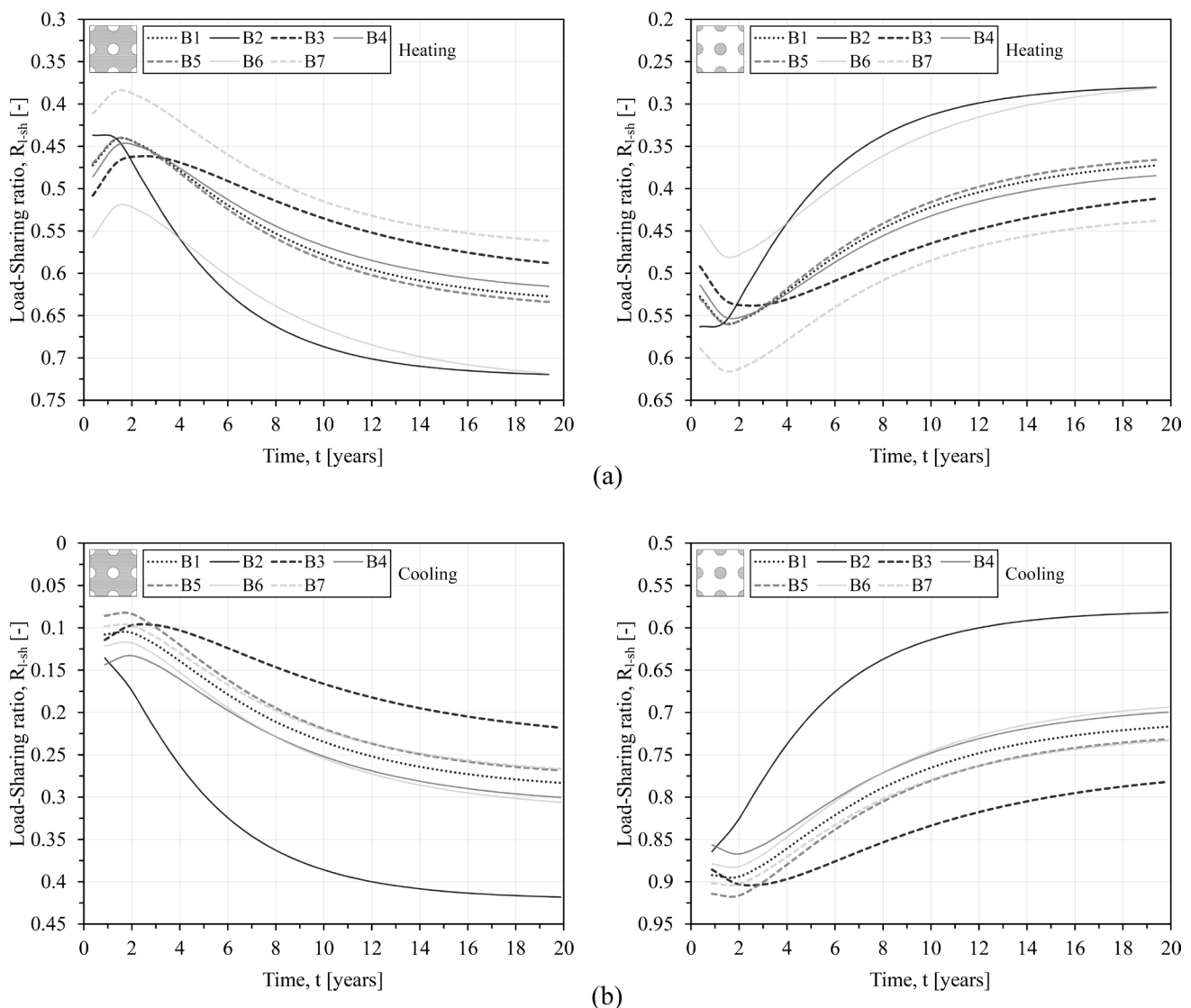


Fig. 10 The temporal evolution of the resultant load transferred to the soil-raft interface and pile heads **a** heating cycles and **b** cooling cycles

contributions of interface stiffness and mechanical loading on stresses, displacements, and load-sharing ratios in a piled raft foundation within stiff saturated clay. The numerical results demonstrated that the constraint level of the system components could significantly influence the foundation's response to thermal loading. The main results can be summarized as follows:

- A change in the foundation constraints altered the stresses; an increase in the constraint as a result of increased soil stiffness and pile-raft connection stiffness led to a larger excess (positive and negative) loads in the piles. This occurs due to the stiffer soil's greater resistance to thermal deformations and the stronger connection's greater reaction stress. However, due to the thermal axial stress being in the elastic range, its magnitude

would not depend on initial stresses in practical applications.

- Regardless of the constraint level, axial stress changes mostly occur at shallow depths due to the significant reaction forces at the pile-raft connection. Moreover, the variation range magnitude at the pile ends was nearly identical in most cases due to the greater constraining effect of the raft and shaft strength than the base strength of floating piles. In the most severe case, the active pile had a thermal axial stress variation of about three times the mechanical axial stress. This suggests that excess stresses should be incorporated into the structural design of piles.
- The consecutive thermal deformations of the piles not only influence the axial stress distribution but also change the mobilized stresses in the soil-pile interface,

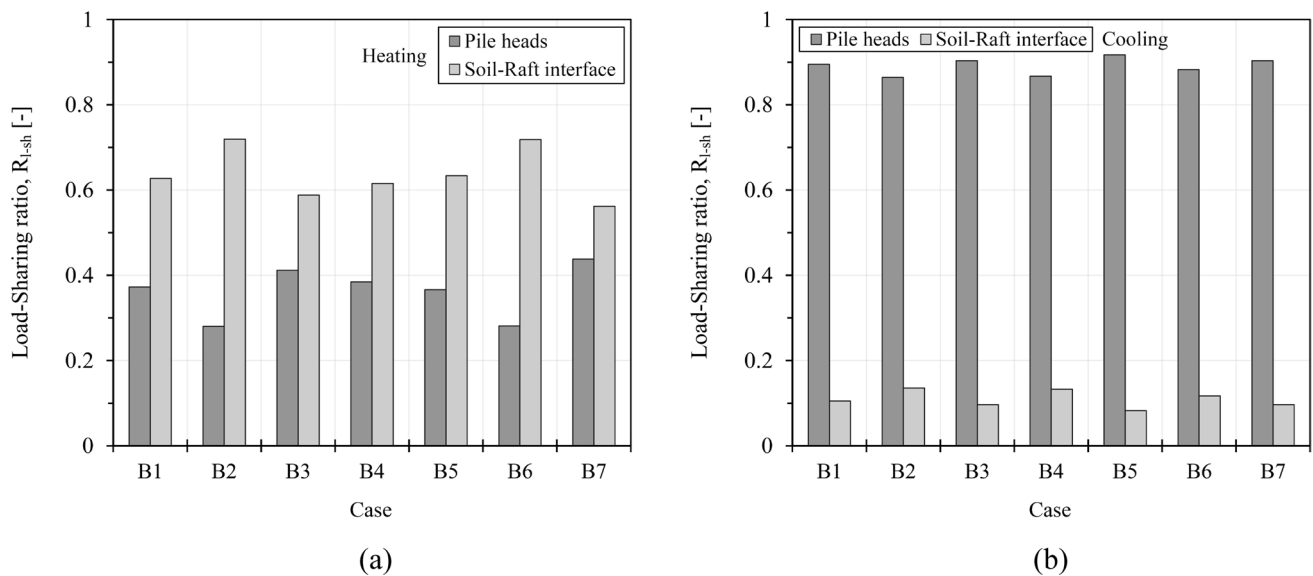


Fig. 11 The limit states of the load distribution **a** heating cycles and **b** cooling cycles

whose mechanism is dependent on the relative pile displacement. It was observed that the contact stress of the pile base increased under thermal loads; however, remobilized shaft strength often declined compared to the initial strength of the shaft. In long-term operations, this phenomenon occurs due to the soil-pile interface's softening and the soil's densification beneath the pile base. The highest pile base contact stress occurred in the softer soil (heating cycles), while the lowest shaft shear stress was observed under the stronger pile-raft connection (cooling cycles).

- The vertical displacement of the raft increased during thermal loading and approached a stabilized excess settlement, which is consistent with the continuous increase in pile base contact stress. However, due to the greater tendency of the soil than the piles to undergo thermal expansion and contraction, the stiffness of the soil-raft interface under a given thermal load was the most influential factor in determining the vertical raft displacement. The highest ultimate excess displacement was obtained nearly one-fifth of the mechanical settlement (in the softer soil), suggesting that the realistic stiffness estimation of the connecting springs is crucial in evaluating superstructure serviceability.
- Due to raft-constrained vertical displacement and the thermal deformation potential difference between the soil and piles, the contact stress of the soil-raft interface increased/decreased in heating/cooling cycles, modifying the resultant load transferred to the pile heads. Therefore, raft penetration into the soil and the stiffness ratio of the pile heads connection to the soil-raft interface could be determinants of the load-sharing

ratios of the system components. The limit state evaluation revealed that the load-sharing ratio of the pile heads varied between one-third and eleven times that of the soil-raft interface.

Acknowledgements Financial support from the Babol Noshirvani University of Technology (Grant No. BNUT/370447/1401) is greatly acknowledged.

Author's contributions Both authors provided intellectual content, edited the manuscript, approved the final version for submission and agree to be accountable for all aspects of the work.

Data availability The authors confirm that the data supporting the findings of this study are available within the article.

Declarations

Conflict of interest On behalf of all authors, the corresponding author states that there is no conflict of interest.

Ethical approval All procedures performed in this study were in accordance with the ethical standards.

Informed consent Informed consent was obtained from all participants.

Code availability The software used in this study is available at <https://www.comsol.com/>.

References

1. Laloui L, Nuth M (2005) Numerical modelling of the behaviour of a heat exchanger pile. *Rev Eur Génie Civ* 9(5–6):827–839

2. Olgun CG (2013) Energy piles: background and geotechnical engineering concepts. In: Proceedings of the 16th Annual George F. Sowers Symposium, Atlanta
3. Rosen MA, Koohi-Fayegh S (2017) Geothermal energy: sustainable heating and cooling using the ground. John Wiley & Sons, New York
4. Laloui L, Rotta Loria AF (2019) Analysis and design of energy geostructures: theoretical essentials and practical application. Academic Press, Cambridge
5. Saggi R (2022) Cyclic pile-soil interaction effects on load-displacement behavior of thermal pile groups in sand. *Geotech Geol Eng* 40(2):647–661
6. Saaly M, Maghoul P (2019) Thermal imbalance due to application of geothermal energy piles and mitigation strategies for sustainable development in cold regions: a review. *Innov Infrastruct Solut* 4(1):1–18
7. Ashrafi MS, Hamidi A (2020) Application of a thermo-elastoplastic constitutive model for numerical modeling of thermal triaxial tests on saturated clays. *Innov Infrastruct Solut* 5(3):1–15
8. Stewart MA, McCartney JS (2014) Centrifuge modeling of soil-structure interaction in energy foundations. *J Geotech Geoenviron Eng* 140(4):04013044
9. Garbellini C, Laloui L (2021) Thermal stress analysis of energy piles. *Géotechnique* 71(3):260–271
10. Lv Z, Kong G, Liu H, Ng CWW (2020) Effects of soil type on axial and radial thermal responses of field-scale energy piles. *J Geotech Geoenviron Eng* 146(10):06020018
11. Cekerevac C, Laloui L (2004) Experimental study of thermal effects on the mechanical behaviour of a clay. *Int J Numer Anal Meth Geomech* 28(3):209–228
12. Di Donna A, Laloui L (2015) Response of soil subjected to thermal cyclic loading: experimental and constitutive study. *Eng Geol* 190:65–76
13. Ng CWW, Ma QJ, Gunawan A (2016) Horizontal stress change of energy piles subjected to thermal cycles in sand. *Comput Geotech* 78:54–61
14. Ng CWW, Ma QJ (2019) Energy pile group subjected to non-symmetrical cyclic thermal loading in centrifuge. *Géotechnique Lett* 9(3):173–177
15. Cunha RP, Bourne-Webb PJ (2022) A critical review on the current knowledge of geothermal energy piles to sustainably climate buildings. *Renew Sustain Energy Rev* 158:112072
16. Mimouni T, Laloui L (2015) Behaviour of a group of energy piles. *Can Geotech J* 52(12):1913–1929
17. Goode JC, McCartney JS (2015) Centrifuge modeling of end-restraint effects in energy foundations. *J Geotech Geoenviron Eng* 141(8):04015034
18. Amatya BL, Soga K, Bourne-Webb PJ, Amis T, Laloui L (2012) Thermomechanical behaviour of energy piles. *Géotechnique* 62(6):503–519
19. Suryatrayastuti ME, Burlon S, Mroueh H (2016) On the understanding of cyclic interaction mechanisms in an energy pile group. *Int J Numer Anal Meth Geomech* 40(1):3–24
20. Olia ASR, Peri'c D (2021) Thermomechanical soil-structure interaction in single energy piles exhibiting reversible interface behavior. *Int J Geomech* 21(5):04021065
21. Rotta Loria AF, Laloui L (2018) Group action effects caused by various operating energy piles. *Géotechnique* 68(9):834–841
22. Ng CWW, Farivar A, Gomaa SMMH, Shakeel M, Jafarzadeh F (2021) Performance of elevated energy pile groups with different pile spacing in clay subjected to cyclic non-symmetrical thermal loading. *Renew Energy* 172:998–1012
23. Farivar A, Jafarzadeh F, Leung AK (2023) Influence of pile head restraint on the performance of floating elevated energy pile groups in soft clay. *Comput Geotech* 154:105141
24. McCartney JS, Murphy KD (2012) Strain distributions in full-scale energy foundations. *DFI J J Deep Found Inst* 6(2):26–38
25. Murphy KD, McCartney JS, Henry KS (2015) Evaluation of thermo-mechanical and thermal behavior of full-scale energy foundations. *Acta Geotech* 10(2):179–195
26. Sutman M, Brettmann T, Olgun CG (2019) Full-scale in-situ tests on energy piles: head and base-restraining effects on the structural behaviour of three energy piles. *Geomech Energy Environ* 18:56–68
27. Fang J, Kong G, Meng Y, Wang L, Yang Q (2020) Thermo-mechanical behavior of energy piles and interactions within energy pile-raft foundations. *J Geotech Geoenviron Eng* 146(9):04020079
28. Wu D, Liu HL, Kong GQ, Ng CWW (2020) Interactions of an energy pile with several traditional piles in a row. *J Geotech Geoenviron Eng* 146(4):06020002
29. Li R, Kong G, Chen Y, Yang Q (2021) Thermomechanical behaviour of an energy pile-raft foundation under intermittent cooling operation. *Geomech Energy Environ* 28:100240
30. Li R, Kong G, Sun G, Zhou Y, Yang Q (2021) Thermomechanical characteristics of an energy pile-raft foundation under heating operations. *Renew Energy* 175:580–592
31. Jeong S, Lim H, Lee JK, Kim J (2014) Thermally induced mechanical response of energy piles in axially loaded pile groups. *Appl Therm Eng* 71(1):608–615
32. Salciarini D, Ronchi F, Cattoni E, Tamagnini C (2015) Thermo-mechanical effects induced by energy piles operation in a small piled raft. *Int J Geomech* 15(2):04014042
33. Saggi R, Chakraborty T (2016) Thermomechanical response of geothermal energy pile groups in sand. *Int J Geomech* 16(4):04015100
34. Di Donna A, Rotta Loria AF, Laloui L (2016) Numerical study of the response of a group of energy piles under different combinations of thermo-mechanical loads. *Comput Geotech* 72:126–142
35. Rotta Loria AF, Laloui L (2017) Thermally induced group effects among energy piles. *Géotechnique* 67(5):374–393
36. Salciarini D, Ronchi F, Tamagnini C (2017) Thermo-hydro-mechanical response of a large piled raft equipped with energy piles: a parametric study. *Acta Geotech* 12(4):703–728
37. Garbellini C, Laloui L (2019) Three-dimensional finite element analysis of piled rafts with energy piles. *Comput Geotech* 114:103115
38. Olia ASR, Peri'c D (2020) Effects of end restraints on thermo-mechanical response of energy piles. *IFCEE* 2021:585–594
39. Pourfakhrian L, Bayesteh H (2020) Effect of slab stiffness on the geotechnical performance of energy piled-raft foundation under thermo-mechanical loads. *Eur J Environ Civ Eng* 26(9):3681–3705
40. Ravera E, Sutman M, Laloui L (2020) Analysis of the interaction factor method for energy pile groups with slab. *Comput Geotech* 119:103294
41. Ravera E, Sutman M, Laloui L (2020) Load transfer method for energy piles in a group with pile-soil-slab-pile interaction. *J Geotech Geoenviron Eng* 146(6):04020042
42. Freitas TMB, Zito M, Bourne-Webb PJ, Sterpi D (2021) Thermal performance of seasonally, thermally-activated floating pile foundations in a cohesive medium. *Eng Struct* 243:112588
43. Amirdehi HA, Shooshpasha I (2022) Evaluation of coupled interaction effects caused by the long-term performance of energy piles in a piled raft foundation. *Geotech Geol Eng* 40(10):5153–5180
44. Sarma K, Saggi R (2020) Implications of thermal cyclic loading on pile group behavior. *J Geotech Geoenviron Eng* 146(11):04020114
45. Ngaradoumbe Nanhorngué R, Pesavento F, Schrefler BA (2013) Sensitivity analysis applied to finite element method model for

- coupled multiphase system. *Int J Numer Anal Meth Geomech* 37(14):2205–2222
46. Asheghi R, Hosseini SA, Saneie M, Shahri AA (2020) Updating the neural network sediment load models using different sensitivity analysis methods: a regional application. *J Hydroinform* 22(3):562–577
 47. COMSOL (2019) COMSOL Multiphysics version 5.4., Burlington
 48. Shahri AA (2016) An optimized artificial neural network structure to predict clay sensitivity in a high landslide prone area using piezocone penetration test (CPTu) data: a case study in southwest of Sweden. *Geotech Geol Eng* 34:745–758
 49. Hawley M, Cuning J (2017) Guidelines for mine waste dump and stockpile design. CSIRO Publishing, Clayton
 50. Shahri AA, Shan C, Larsson S (2022) A novel approach to uncertainty quantification in groundwater table modeling by automated predictive deep learning. *Nat Resour Res* 31(3):1351–1373
 51. Brandl H (2006) Energy foundations and other thermo-active ground structures. *Géotechnique* 56(2):81–122
 52. Andersland OB, Ladanyi B (2013) An introduction to frozen ground engineering. John Wiley & Sons, New York
 53. Das BM, Sivakugan N (2018) Principles of foundation engineering. Cengage learning, Boston
 54. Bourne-Webb PJ, Amatya B, Soga K, Amis T, Davidson C, Payne P (2009) Energy pile test at Lambeth College, London: geotechnical and thermodynamic aspects of pile response to heat cycles. *Géotechnique* 59(3):237–248
 55. Day RW (2010) Foundation engineering handbook: design and construction with the 2009 international building code. McGraw-Hill Education, New York
 56. Carter M, Bentley SP (1991) Correlations of soil properties. Pentech Press Publishers, London
 57. El-Reedy MA (2019) Offshore structures: design, construction and maintenance. Gulf Professional Publishing, Houston
 58. Ng CWW, Mu QY, Zhou C (2017) Effects of boundary conditions on cyclic thermal strains of clay and sand. *Géotechnique Lett* 7(1):73–78
 59. Olgun CG, Ozudogru TY, Arson C (2014) Thermo-mechanical radial expansion of heat exchanger piles and possible effects on contact pressures at pile-soil interface. *Géotechnique Lett* 4(3):170–178
 60. Briaud JL (2013) Geotechnical engineering: unsaturated and saturated soils. John Wiley & Sons, New York
 61. Rotta Loria AF, Bocco M, Garbellini C, Muttoni A, Laloui L (2020) The role of thermal loads in the performance-based design of energy piles. *Geomech Energy Environ* 21:100153
 62. Phoon KK, Cao ZJ, Ji J, Leung YF, Najjar S, Shuku T, Tang C, Yin ZY, Ikumasa Y, Ching J (2022) Geotechnical uncertainty, modeling, and decision making. *Soils Found* 62(5):101189

Springer Nature or its licensor (e.g. a society or other partner) holds exclusive rights to this article under a publishing agreement with the author(s) or other rightsholder(s); author self-archiving of the accepted manuscript version of this article is solely governed by the terms of such publishing agreement and applicable law.